Shaken and stirred: the effects of turbulence and rotation on disc and outflow formation during the collapse of magnetized molecular cloud cores

Benjamin T. Lewis⋆ and Matthew R. Bate⋆

School of Physics and Astronomy, University of Exeter, Stocker Road, Exeter EX4 4QL, UK

ABSTRACT

We present the results of 18 magnetohydrodynamical calculations of the collapse of a molecular cloud core to form a protostar. Some calculations include radiative transfer in the flux-limited diffusion approximation, while others employ a barotropic equation of state. We cover a wide parameter space, with mass-to-flux ratios ranging from $\mu = 5$ to 20; initial turbulent amplitudes ranging from a laminar calculation (i.e. where the Mach number, $\mathcal{M} = 0$) to transonic $\mathcal{M} = 1$; and initial rotation rates from $\beta_{\rm rot} = 0.005$ to 0.02. We first show that using a radiative transfer scheme produces warmer pseudo-discs than the barotropic equation of state, making them more stable. We then 'shake' the core by increasing the initial turbulent velocity field, and find that at all three mass-to-flux ratios transonic cores are weakly bound and do not produce pseudo-discs; $\mathcal{M} = 0.3$ cores produce very disrupted discs; and $\mathcal{M} = 0.1$ cores produce discs broadly comparable to a laminar core. In our previous paper, we showed that a pseudo-disc coupled with sufficient magnetic field is necessary to form a bipolar outflow. Here, we show that only weakly turbulent cores exhibit collimated jets. We finally take the $\mathcal{M} = 1.0$, $\mu = 5$ core and 'stir' it by increasing the initial angular momentum, finding that once the degree of rotational energy exceeds the turbulent energy in the core the disc returns, with a corresponding (though slower), outflow. These conclusions place constraints on the initial mixtures of rotation and turbulence in molecular cloud cores which are conducive to the formation of bipolar outflows early in the star formation process.

Key words: accretion, accretion discs – MHD – radiative transfer – turbulence – stars: formation – stars: winds, outflows.

1 INTRODUCTION

Chaotic, turbulent, molecular clouds are the birthplaces of stars (Padoan & Nordlund 2002; McKee & Ostriker 2007). These large clouds evolve and ultimately structures therein (André et al. 2010; Men'shchikov et al. 2010; Ward-Thompson et al. 2010; Myers 2009) succumb to the Jeans (1902) instability and collapse – creating the molecular cloud cores that ultimately form protostars (Shu 1977; Motte & André 2001). Many open questions in astronomy are related to how these cores evolve, for example, how are multiple star systems formed and the related question of how the very large initial angular momentum of the core is reduced to the stellar angular momenta observed in fully evolved systems (Li, Krasnopolsky & Shang 2013). Molecular clouds are comprised of a magnetized astrophysical plasma (Crutcher 2012; Heyer & Dame 2015) which results in magnetic effects playing an important role in the col-

lapse of the cloud cores. Ultimately, once these cores collapse to protostellar densities, jets and other outflows are produced. These outflows, and particularly collimated jets, transport angular momentum away from the protostellar core and can therefore explain why stars are not observed to be rotating close to their break-up speed. Consequently, an understanding of how the initial conditions in the molecular core affect the generation of outflows is an important area of study.

The gas within a galaxy is invariably turbulent (Roberts 1969). Consequently, the molecular gas within a cloud also is; as seen, for example, in the Horsehead nebula (Pound, Reipurth & Bally 2003; Hily-Blant et al. 2005), and also more generally (Heyer & Brunt 2004). These turbulent conditions must then cascade down to the scales of molecular cloud cores. In the process, the magnitude of the turbulence will decay from being supersonic (in a molecular cloud) to transonic or sub-sonic in the core. Several numerical calculations, including Larson (1981), Klessen, Heitsch & Mac Low (2000), Mac Low & Klessen (2004), and Bate (2009, 2012) have demonstrated that the turbulent motions within the cloud are an essential part

⋆ E-mail: benjamin.lewis@rit.edu (BTL); mbate@astro.ex.ac.uk (MRB)

of its evolution. These motions produce a filamentary structure and then localized overdensities which can collapse and form stars (Elmegreen 1993).

In our previous works, Lewis, Bate & Price (2015) and Lewis & Bate (2017), we explored how the gravitational collapse of magnetized molecular cloud cores is affected by changing the geometry and strength of the initial magnetic field. However, all of the calculations presented in those two works used cloud cores which, although rotating, had completely laminar velocity fields. These two papers continued a long series of work in this field including Tomisaka (2002), Matsumoto & Tomisaka (2004), Banerjee & Pudritz (2006), Price & Bate (2007), Machida, Inutsuka & Matsumoto (2008), Ciardi & Hennebelle (2010), Bate, Tricco & Price (2014), and Kuruwita, Federrath & Ireland (2017). Most recently, although not discussed in this paper, attention has turned to including non-ideal magnetohydrodynamic effects (e.g. Machida, Inutsuka & Matsumoto 2006, 2007; Pandey & Wardle 2008; Wurster, Price & Ayliffe 2014,, Tsukamoto et al. 2015; Tomida, Okuzumi & Machida 2015; Wurster, Price & Bate 2016).

In this work, we present the results of a series of calculations involving turbulent cores with the same turbulent power spectrum as used in Bate (2009) et seq. and thereby bridge the gap between simulations of whole molecular clouds and of fully formed protostellar objects. This choice is also consistent with Burkert & Bodenheimer (2000), who proposed that the observed linewidths of molecular cloud cores could be caused by turbulent motion following a power law (i.e. where the wavenumber of the turbulence, k, follows $P(k) \propto k^n$) with $n \in [-3, -4]$. We show that the initial velocity field of a molecular cloud core has as important an impact as the initial magnetic field strength – both of which are seeded by the overall molecular cloud. In addition, we show that the initial angular momentum of the cloud is closely linked to the nature of any protostellar outflows (along with the magnetic field strength and geometry, as we observed in Lewis et al. 2015).

We present the results of an ensemble of 18 smoothed particle radiation magnetohydrodynamical (SPRMHD) calculations of the collapse of a one solar mass molecular cloud core. Each core studied has a different set of initial conditions, ranging from being almost laminar to transonic cores, and covering different initial angular momenta. We also take the opportunity to compare the use of an approximate barotropic equation of state with a flux-limited diffusion (FLD) radiative transfer (RT) scheme.

In Section 2, we set out our numerical SPRMHD scheme, and in Section 3, we discuss the initial conditions used for the ensemble of calculations. In Section 4, we compare the results from calculations using the barotropic equation of state with the full FLD RT scheme. Following this, in Sections 5–7, we discuss the common early phase of the collapse, the effect of increasing turbulence, and the effect of increasing angular momentum on the subsequent evolution of the core, respectively. We then compare these results both to observations and existing theoretical work in Section 8. Finally, our conclusions are summarized in Section 9.

2 METHOD

Turbulent magnetized plasmas can only be explored using a numerical scheme. Therefore, these calculations are evolved by solving the equations of (flux-limited) radiation ideal magnetohydrodynamics (MHD) with self-gravity, which comprise

$$D_t \rho = -\rho \nabla^i v^i, \tag{1}$$

$$D_t v^i = -\frac{1}{\rho} \nabla^i \left(p + \frac{1}{8\pi} B^2 \right) \delta^{ij}$$
$$+ \frac{1}{4\pi} \frac{1}{\rho} \nabla^i B^i B^j - \nabla^i \phi + \frac{\kappa F^i}{c}, \tag{2}$$

$$D_t \frac{B^i}{\rho} = \left(\frac{B^j}{\rho} \nabla^j \right) v^i, \tag{3}$$

$$D_t \frac{E}{\rho} = -\frac{1}{\rho} \nabla^i F^i - \frac{1}{\rho} \nabla^i v^j P^{ij} + 4\pi \kappa B(T_{\text{fl}}) - c\kappa E, \tag{4}$$

$$D_t u = -\frac{p}{\rho} \nabla^i v^i - 4\pi \kappa B(T_{\text{fl}}) + c\kappa E, \tag{5}$$

$$\triangle \phi = 4\pi G \rho. \tag{6}$$

In equations (1)–(6) and the rest of this paper,

$$D_t \equiv \partial_t + v^i \nabla^i \tag{7}$$

denotes the convective derivative operator, with ∂_t being the partial derivative with respect to time, $\triangle$ is the Laplacian operator; ρ, p, v^i, B^i, F^i, E, and ϕ are the density, hydrodynamic fluid pressure, velocity, magnetic, radiative flux, radiation energy density, and gravitational potential fields respectively; u is the specific energy of the fluid; P^{ij} is the radiation pressure tensor; κ is the fluid opacity; $c = 2.9979 \times 10^{10}\,\text{cm s}^{-1}$ is the speed of light in vacuo; and $G = 6.6726 \times 10^{-8}\,\text{dyn cm}^2\,\text{g}^{-2}$ is the gravitational constant. Repeated indices imply summation. We assume that the fluid is always in local thermodynamic equilibrium. As a consequence, we incorporate the emission of radiation by the fluid using the Planck (1914) function

$$B(T_{\text{fl}}) = \frac{\sigma_B T_{\text{fl}}^4}{\pi}, \tag{8}$$

where $\sigma_B = 5.6705 \times 10^{-5}\,\text{erg cm}^{-2}\,\text{s}^{-1}\,\text{K}^{-4}$ is the Stefan–Boltzmann constant and T_{fl} is the temperature of the fluid. An additional temperature – the radiation temperature, T_{rad}, is also defined as

$$E = \frac{4\sigma_B T_{\text{rad}}^4}{c}. \tag{9}$$

The large number of physical properties evolved requires an array of different numerical approaches. We start by discretizing these equations by using a smoothed particle radiation MHD scheme, originally invented by Lucy (1977) and Gingold & Monaghan (1977) and as set out for ideal MHD by Price & Monaghan (2004a, 2005) and then extend this basic method as follows.

To ensure the efficient use of resolution and therefore computational resources, we use a self-consistent variable smoothing length, h, scheme (Price & Monaghan 2004b) where

$$h = \eta \left(\frac{m}{\rho} \right)^{\frac{1}{\nu}}, \tag{10}$$

where m is the mass of the smoothed particle hydrodynamics (SPH) particle, $\eta = 1.2$ for the cubic B-spline kernel (Monaghan 1985), and $\nu = 3$ is the number of spatial dimensions. The typical number of neighbour particles is then $N_{\text{ngh}} \sim 53$.

The MHD scheme given in Price & Monaghan (2004a, 2005) is unstable in certain numerical situations (see Lewis, Bate & Tricco 2016). We stabilize the momentum equation against the tensile pairing instability using the source term correction proposed by Børve, Omang & Trulsen (2001) with the parameter χ (see the discussions in Tricco & Price 2012; Lewis et al. 2016) fixed at 1. The induction equation in SPMHD does not maintain the solenoidal

constraint – i.e. that $\nabla^i B^i = 0$. In previous work, we used the constrained hyperbolic divergence cleaning proposed by Tricco & Price (2012) based on the earlier grid-based method of Dedner et al. (2002). In this work, we adopt an improvement of this technique, detailed in Tricco, Price & Bate (2016), which is invariant to gradients in the magnetosonic wave velocity of the fluid. As before we couple a scalar field, ψ, to the induction equation such that

$$D_t B^i \big|_{\nabla^i B^i} = -\nabla^i \psi. \tag{11}$$

However, we instead evolve ψ/c_c as opposed to simply ψ according to

$$D_t \frac{\psi}{c_c} = -c_c^2 \nabla^i B^i - \frac{\psi}{\tau} - \frac{1}{2} \psi \left(\nabla^i v^i \right). \tag{12}$$

We set the cleaning wave speed, c_c, to the fastest magnetosonic wave velocity, i.e.

$$c_c^2 = c_s^2 + c_a^2 = c_s^2 + \frac{B^2}{4\pi\rho}, \tag{13}$$

where c_s and c_a are the sound and Alfvén speeds of the fluid, and set the damping time-scale to

$$\tau = \frac{h}{\sigma_c c_c}, \tag{14}$$

with $\sigma_c = 4/5$ so that the cleaning wave is critically damped. These two additions effectively stabilize our MHD method for the duration of our calculations.

To prevent interparticle penetration and to capture shocks in the fluid, we add an artificial viscosity term to the momentum equation, and to capture discontinuities in the magnetic field, we add an artificial resistivity term to the induction equation (and therefore our method is actually quasi-ideal MHD). We use the Riemann solver-based artificial viscosity term of Monaghan (1997) with a switch (Morris & Monaghan 1997) to reduce dissipation when the viscosity term is unnecessary with the parameter $\alpha_{AV} \in [0.1, 1.0]$. For the artificial resistivity, we use the switch proposed in Tricco & Price (2013) with the parameter $\alpha_{AR} \in [0.0, 1.0]$.

Self-gravitational forces are computed using a binary tree and we also use this tree to find the list of neighbour particles (Benz et al. 1990; Benz 1988). The gravitational potential itself is then softened using the ordinary SPH smoothing kernel, varying with smoothing length as in equation (10) (Price & Monaghan 2007).

Equations (2), (4), and (5) contain radiation hydrodynamic components where

$$F^i = -\frac{c\lambda(R)}{\kappa\rho} \nabla^i E. \tag{15}$$

This describes a fluid and radiation (i.e. two-temperature) FLD RT scheme. We evolve this RT scheme using the same implicit method as in Whitehouse, Bate & Monaghan (2005), Whitehouse & Bate (2006), and Bate et al. (2014). We use the flux limiter (Levermore & Pomraning 1981)

$$\lambda(R) = \frac{2+R}{6+3R+R^2}, \tag{16}$$

where

$$R = \left| \frac{\nabla^i E}{\kappa\rho E} \right|, \tag{17}$$

with the opacity represented by κ. We obtain values of κ from the opacity tables of Alexander (1975) and Pollack, McKay & Christofferson (1985) as detailed in Whitehouse & Bate (2006). This allows the temperature evolution of the fluid to be calculated

and evolved – high-density hot fluid regions will radiate and transfer energy to their cooler surroundings. The Eddington tensor,

$$f^{ij} = \frac{1}{2} [1 - f(E)] \delta^{ij} + \frac{1}{2} [3f(E) - 1] \hat{n}^i \hat{n}^j, \tag{18}$$

can be used to calculate the radiation pressure from the radiation energy density

$$P^{ij} = f^{ij} E. \tag{19}$$

Finally, the Eddington factor function, $f(E)$, in equation (18) and the flux limiter in equation (16) are connected by the relation

$$f(E) = \lambda(R) + \lambda^2(R) R^2(E). \tag{20}$$

Two equations of state are used in this paper. In most of the calculations presented in this paper, we use the radiative equation of state (see Whitehouse & Bate 2006) given by

$$P(\rho, T_{fl}) = \frac{\mathcal{R}}{\mu_{mol}} \rho T_{fl}, \tag{21}$$

where the gas constant is given by $\mathcal{R} = 8.3145 \times 10^7$ erg K^{-1} mol^{-1}, we use a mean molecular weight of $\mu_{mol} = 2.38$ and the fluid temperature $T_{fl} = u/C_v$, where C_v represents the isochoric specific heat capacity. The mean molecular weight and heat capacity used represent a mixture of hydrogen and helium and incorporate the effects of hydrogen dissociation and the ionization of hydrogen and helium, but does not include any contribution from metals (see Black & Bodenheimer 1975). In some calculations, we use the barotropic equation of state given by (cf. Machida et al. 2008)

$$P(\rho) = c_{s,0}^2 \begin{cases} \rho & \rho \leq \rho_{c,1} \\ \rho_{c,1} \left(\frac{\rho}{\rho_{c,1}} \right)^{\frac{7}{5}} & \rho_{c,1} < \rho \leq \rho_{c,2} \\ \rho_{c,1} \left(\frac{\rho_{c,2}}{\rho_{c,1}} \right)^{\frac{7}{5}} \left(\frac{\rho}{\rho_{c,2}} \right)^{\frac{11}{10}} & \rho > \rho_{c,2}, \end{cases} \tag{22}$$

where $c_{s,0}$ represents the initial sound speed of the calculation and with critical densities of $\rho_{c,1} = 10^{-14}$ g cm^{-3} and $\rho_{c,2} = 10^{-10}$ g cm^{-3} to allow us to compare an approximate treatment with the full FLD RT scheme. The physical consequences of the choice of critical densities were discussed in Lewis & Bate (2017).

The entire SPRMHD detailed here is then temporally evolved using a second-order Runge–Kutta–Fehlberg integrator (denoted RK2(4) in Fehlberg 1969). Each SPH particle has an individual time-step so that particles in lower density or otherwise numerically simpler regions use fewer computational resources.

Sink particles (Bate, Bonnell & Price 1995) are inserted when the density in the simulation exceeds either $\rho_{crit} = 10^{-10}$ g cm^{-3} or 10^{-5} g cm^{-3}, depending on the specific initial conditions. In an RT calculation, the standard sink particle insertion tests are disabled (for instance sinks may be inserted with a non-negative $\nabla^i \dot{v}^i$). The sink particle insertion tests of Bate et al. (1995) were designed to ensure that the region where $\rho \geq \rho_{crit}$ was undergoing gravitational collapse. However, when wishing to insert a sink particle within a first hydrostatic core using an accretion radius that is smaller than the first core, the region being replaced is not collapsing (it is hydrostatic) and, in fact, is not self-bound (i.e. the external pressure matters). Thus, the tests are disabled. This can, however, cause spurious fragmentation if the critical density is too low. For the calculations in this paper, choosing $\rho_{crit} = 10^{-10}$ g cm^{-3} is sufficient to avoid spurious fragmentation for slowly rotating cores, but may produce spurious fragmentation in more rapidly rotating

cores where the highest density regions are more extended. Therefore, for the calculations with an initial solid-body rotation rate of $\geq 3.54 \times 10^{-13}\,\mathrm{rad\,s^{-1}}$, we delay the insertion of sinks until after the second collapse phase to prevent spurious fragmentation. Since the slowly rotating cases only produce a single sink particle, raising the critical density in these calculations would have no significant effect other than to increase the computational time.

We set the accretion radius of the sink particles to $r_{\mathrm{acc}} = 1\,\mathrm{au}$ (for both critical densities). Any SPH particles that fall within this distance of a sink particle are removed from the simulation and their masses are added to the sink if the usual checks for boundness detailed in Bate et al. (1995) are passed. We impose a further inner boundary at $0.1\,\mathrm{au}$ within which particles are accreted unconditionally to prevent small time-steps arising from large gravitational accelerations close to the sink particle. Our choice of accretion radius is a compromise between numerical efficiency – a larger radius results in a shorter run-time – and incorporating as much of the first hydrostatic core as possible (a first hydrostatic core has a typical radius of $\approx 4\,\mathrm{au}$, Larson 1969). Previous work (viz. Price, Tricco & Bate 2012; Lewis, Bate & Price 2015) has shown that reducing the radius from 5 to 1 au increases the jet velocity slightly from $|v_z| \approx 5$ to $8\,\mathrm{km\,s^{-1}}$, but has no other significant effect.

Other than through gravity, the sink particles do not interact with other SPH particles: importantly they do not emit radiation (they are 'cold') and have no magnetic field components. Since the sink particle has no magnetic field, the field carried by any accreted particle is effectively destroyed, i.e. eliminated from the calculation rather than incorporated into the properties of the sink particle. The physical consequences of this infelicity have been discussed previously (e.g. by Lewis et al. 2016), and the primary effect on the calculation is to render a robust divergence cleaning scheme even more essential.

The calculations were performed using SPHNG, a three-dimensional hybrid MPI and OPENMP smoothed particle radiation MHD code originating from Benz (1990) and subsequently significantly modified by Bate et al. (1995), Whitehouse & Bate (2006), Price & Bate (2007), and others. Each individual calculation was completed on a pair of 6-core hyperthreaded CPUs (giving a total of 24 execution threads), taking between 16 and 32 d of wall time (approximately 553 000 and 1 100 000 core hours) depending on the initial conditions used.

3 INITIAL CONDITIONS

We adopt initial conditions that are broadly similar to Lewis & Bate (2017) , which follow the general approach seen in Price et al. (2012), Bate et al. (2014), Lewis et al. (2015), and others. However, in contrast to these works, we add a turbulent velocity field and also vary the initial angular momentum of the molecular cloud core.

A cold uniform density sphere of SPH particles is placed within a warm low-density container medium with the SPH particles initially placed on a cubic lattice, and the whole structure is then placed in a periodic box. This numerical set-up is similar to that used by Hosking (2002); alternative arrangements which use, for example, Bonnor–Ebert spheres (Bonnor 1956; Ebert 1955) instead of a uniform density distribution include Banerjee & Pudritz (2006). We use ca. 3×10^6 SPH particles for the sphere (this is double the mass resolution in Lewis et al. 2015 and Lewis & Bate 2017) and which represents the molecular cloud core, and ca 1.5×10^6 particles for the surrounding medium. The core has a radius of $r_{\mathrm{core}} = 4 \times 10^{16}\,\mathrm{cm}$ and a mass of $M_{\mathrm{core}} = 1\,\mathrm{M_\odot}$, giving an initial uniform density of $\rho_{\mathrm{core},\,0} = 7.4 \times 10^{-18}\,\mathrm{g\,cm^{-3}}$. The initial sound speed of the core is

set to $c_{\mathrm{s},\,0} = 2.2 \times 10^4\,\mathrm{cm\,s^{-1}}$ giving the core an initial fluid temperature of $T_{\mathrm{fl,\,core},0} = 13.8\,\mathrm{K}$. The core and container medium are in pressure equilibrium so the low-density container medium has an initial fluid temperature of $\approx 400\,\mathrm{K}$. When using RT, the radiation temperature, T_{rad}, is initialized to 13.8 K in both regions. Both the values of the fluid and radiation temperatures are held constant in the container medium throughout the calculations.

Our mass resolution significantly exceeds the resolution criteria in Bate & Burkert (1997) (which require a Jean's mass be resolved by at least $2N_{\mathrm{ngh}}$ particles) but also ensures that we correctly capture magnetized turbulence since Federrath et al. (2011) observed this requires significantly higher resolution than that required in hydrodynamic problems.

The initial magnetic field is set uniformly throughout the core and container medium and is aligned to the z-axis (so $\vartheta = 0°$ and $B_0^z = B_0$; Lewis et al. 2015). The initial magnetic field strength is set according to the dimensionless mass-to-flux ratio, μ, which is defined as

$$\mu = \frac{\varpi_{\mathrm{core}}}{\varpi_{\mathrm{crit}}}. \tag{23}$$

The ratio between the magnetic pressure and self-gravitational forces, ϖ_{core}, in a magnetized sphere is given by

$$\varpi_{\mathrm{core}} = \frac{M_{\mathrm{core}}}{\pi\, r_{\mathrm{core},0}^2\, B_0}, \tag{24}$$

and the 'critical' ratio at which these forces are in balance is given by

$$\varpi_{\mathrm{crit}} = \frac{c_1}{3\pi}\sqrt{\frac{5}{G}} \approx 490\,\mathrm{g\,G^{-1}\,cm^{-2}}, \tag{25}$$

where we use $c_1 = 0.53$ as determined by Mouschovias & Spitzer (1976). The field is periodic across the box, and continuous between the core and surrounding medium. This prevents numerical artefacts at the edge of the core even in very turbulent calculations.

The surrounding medium has zero initial velocity. The initial velocity profile of the core is produced by combining a turbulent component, v_{turb}^i, and a solid-body rotation component, v_{rot}^i, i.e.

$$v^i = v_{\mathrm{turb}}^i + v_{\mathrm{rot}}^i. \tag{26}$$

In contrast, Lewis et al. (2015), Lewis & Bate (2017), etc., only used a rotation component. To make comparisons with other calculations simpler, we use two dimensionless parameters, β_{turb} and β_{rot} representing the ratio of turbulent and rotational energy to gravitational potential energy, respectively, to set the velocity field. These parameters are defined as

$$\beta_{\mathrm{rot}} = \frac{1}{3}\frac{r_{\mathrm{core},0}^3 \Omega_0^2}{G M_{\mathrm{core},0}}, \tag{27}$$

where Ω_0^2 is the initial angular velocity of the core, and

$$\beta_{\mathrm{turb}} = \frac{1}{2}\frac{r_{\mathrm{core},0}\,\bar{v}_{\mathrm{turb}}^2}{G M_{\mathrm{core},0}}. \tag{28}$$

$\bar{v}_{\mathrm{turb}}$ is the root mean square (rms) velocity of the turbulence, since the velocity of any individual particle will vary according to the Gaussian normal distribution discussed below, and is related to the Mach number, $\mathcal{M}$, of the turbulence via

$$\bar{v}_{\mathrm{turb}} = \mathcal{M}c_{\mathrm{s}}, \tag{29}$$

where c_{s} is the sound speed of the fluid (which is initially spatially constant). We also define the ratio of magnetic energy to

Table 1. Initial conditions for the calculations presented in this paper. μ is the mass-to-flux ratio (see equation 23), B_0 is the initial magnetic field strength, $\mathcal{M}$ is the initial turbulent Mach number, Ω_0 is the initial angular speed of the core; β_{mag}, β_{turb}, and β_{rot} are the ratios of magnetic, turbulent kinetic, and rotational kinetic energy to gravitational energy (equations 27, 28, and 30), and β_{tot} is the ratio of all the non-thermal supporting energy sources to the gravitational energy (equation 31). Note that calculations μ05–M10–r001(R) and μ05–M10–r002(R) use $\rho_{crit} = 10^{-5}\,\mathrm{g\,cm^{-3}}$, and all other calculations use $\rho_{crit} = 10^{-10}\,\mathrm{g\,cm^{-3}}$ as the critical density for sink particle creation. $\alpha_0 = 0.45$ (see equation 32) throughout.

Calculation name	Equation of state	μ	B_0 [μG]	β_{mag}	$\mathcal{M}$	β_{turb}	Ω_0 [$\times 10^{-13}\mathrm{rad\,s^{-1}}$]	β_{rot}	β_{tot}	$\alpha_0 + \beta_{tot}$
μ05–M00(R)	FLD RT	5	163	0.071	0	0	1.77	0.005	0.076	0.526
μ05–M01(M)	Barotropic	5	163	0.071	0.1	0.0013	1.77	0.005	0.077	0.527
μ05–M01(R)	FLD RT	5	163	0.071	0.1	0.0013	1.77	0.005	0.077	0.527
μ05–M03(M)	Barotropic	5	163	0.071	0.3	0.012	1.77	0.005	0.088	0.538
μ05–M03(R)	FLD RT	5	163	0.071	0.3	0.012	1.77	0.005	0.088	0.538
μ05–M10(M)	Barotropic	5	163	0.071	1.0	0.13	1.77	0.005	0.206	0.656
μ05–M10(R)	FLD RT	5	163	0.071	1.0	0.13	1.77	0.005	0.206	0.656
μ05–M10–r001(R)	FLD RT	5	163	0.071	1.0	0.13	3.54	0.01	0.211	0.661
μ05–M10–r002(R)	FLD RT	5	163	0.071	1.0	0.13	7.08	0.02	0.221	0.671
μ10–M00(R)	FLD RT	10	81	0.018	0	0	1.77	0.005	0.023	0.473
μ10–M01(R)	FLD RT	10	81	0.018	0.1	0.0013	1.77	0.005	0.024	0.474
μ10–M03(R)	FLD RT	10	81	0.018	0.3	0.012	1.77	0.005	0.035	0.485
μ10–M10(R)	FLD RT	10	81	0.018	1.0	0.13	1.77	0.005	0.153	0.603
μ20–M00(R)	FLD RT	20	41	0.0045	0	0	1.77	0.005	0.0095	0.460
μ20–M01(R)	FLD RT	20	41	0.0045	0.1	0.0013	1.77	0.005	0.0108	0.461
μ20–M03(R)	FLD RT	20	41	0.0045	0.3	0.012	1.77	0.005	0.0215	0.472
μ20–M10(M)	Barotropic	20	41	0.0045	1.0	0.13	1.77	0.005	0.140	0.590
μ20–M10(R)	FLD RT	20	41	0.0045	1.0	0.13	1.77	0.005	0.140	0.590

gravitational potential energy as

$$\beta_{mag} = \frac{5}{18}\frac{B^2 r_{core,0}^4}{GM^2} \tag{30}$$

Using this we obtain values of $\beta_{mag} = 0.071, 0.018,$ and 0.0045 for $\mu = 5, 10,$ and 20 respectively. We can then define the ratio of all the forms of non-thermal support – magnetic pressure, turbulent kinetic, and rotational energy – against the gravitational self-potential as

$$\beta_{tot} = \beta_{mag} + \beta_{turb} + \beta_{rot}. \tag{31}$$

Using this, we obtain values of β_{tot} ranging from 0.0095 for a $\mu = 20$, $\mathcal{M} = 0.1$ calculation to 0.221 for $\mu = 5$, $\mathcal{M} = 1.0$, $\beta_{rot} = 0.02$ calculation, i.e. ranging from a very supercritical core to one which less strongly bound. Our range of values of β_{rot}, from 0.005 to 0.02, is consistent with Goodman et al. (1993) (see in particular, the distribution in fig. 11 therein), albeit with slightly less angular momentum than proposed by Burkert & Bodenheimer (2000).

For completeness, we can also calculate the ratio of thermal energy to the magnitude of the gravitational potential energy as

$$\alpha_0 = \frac{5}{2}\frac{\mathcal{R}T_{fl}r_{core,0}}{\mu_{mol}GM}. \tag{32}$$

In all the calculations presented in this paper, we have $\alpha_0 = 0.45$. The sum, $\alpha_0 + \beta_{tot}$ ranges from 0.460 to 0.671, i.e. from reasonably bound to a more weakly bound core. In a turbulent calculation, it is likely that there will be regions, even in a core with $\alpha_0 + \beta_{tot} = 0.671$, where locally the turbulent amplitude is sufficient to cause material to unbind. Conversely, although not covered in this paper, even if the sum $\alpha_0 + \beta_{tot} > 1$ there would likely be regions where the local turbulence is *low* enough that these regions would remain bound.

The rotational component of the velocity field is provided by solid body rotation about the *z*-axis. The turbulent component is provided by giving every particle in the core an initial velocity at $t = 0$ – the turbulence is not driven and therefore decays over time. We im-

pose turbulence in a similar manner to Ostriker, Stone & Gammie (2001) and Bate, Bonnell & Bromm (2003). A uniform 128^3 grid of velocities was generated and the initial particle velocities were interpolated from this, multiplied by a co-efficient to produce the correct overall turbulent Mach number. The generated grid represents a divergence-free (i.e. our turbulence is not compressive, cf. Federrath et al. 2010) random Gaussian field with a power spectrum which follows $P(k) \propto k^{-4}$, where k is the wavenumber, consistent with Burkert & Bodenheimer (2000). The velocity dispersion, σ, of such a distribution follows scaling law of Larson (1981), with $\sigma(r) \propto \sqrt{r}$, where r is the distance.

We note that our initial conditions differ from Matsumoto, Machida & Inutsuka (2017), which use a Bonnor–Ebert sphere and apply *only* an initially turbulent velocity field, rather than a superposition of a turbulent and a rotational field.

This provides a wide range of potential initial conditions which can be explored. We present 18 calculations in total, with the initial conditions as set out in Table 1. These calculations span mass-to-flux ratios from $\mu = 5$ to 20, turbulent velocities from $\mathcal{M} = 0$ (a laminar core) to $\mathcal{M} = 1$ (a transonic core), rotational velocities from $\beta_{rot} = 0.005$ to 0.02, and include both barotropic and FLD RT formalisms. In this way, we sample a wide area of the parameter space, from a tightly bound, weakly magnetized, laminar core to weakly bound, transonic, strongly magnetized, and rapidly rotating core.

4 DEPENDENCE OF THE RESULTS ON THE EQUATION OF STATE

All the molecular cloud cores studied here are supercritical, and therefore the self-gravity of the gas will cause the core to centrally collapse. As a characteristic time, we use the free-fall time of a initially motionless (i.e. non-rotating and laminar), non-magnetized, sphere, so that for a core with mass $M_{core} = 1\,\mathrm{M_\odot}$ and $t_{ff} = 24\,400$ yr. This is in effect a lower bound on how long the core will take to
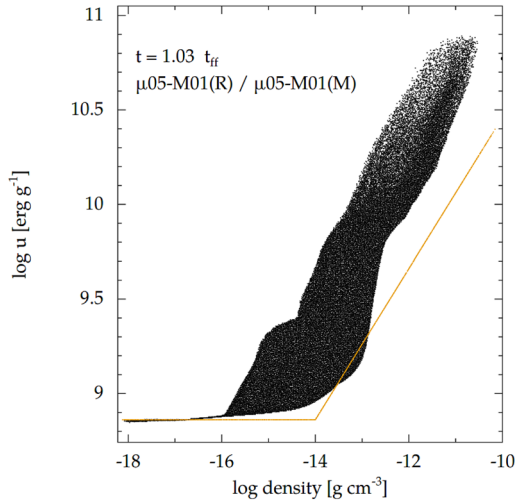
Figure 1. Specific internal energy, u, as a function of the fluid density at $t = 1.03\,t_{\rm ff}$ for all SPH particles within core of the μ05–M01(R) calculation (black dots) and μ05–M01(M) calculation (orange dots). The RT scheme causes a generally greater, and earlier, increase in u compared to the barotropic equation of state. The latter is fixed until the first critical density ($\rho = 1 \times 10^{-14}\,{\rm g\,cm^{-3}}$) is reached and linear thereafter; if regions of the fluid were to exceed the second critical density the slope of this line would change. The RT scheme is not a simple function of the density however (see e.g. the 'knee' in the temperature distribution between $\rho \approx 1 \times 10^{-13}$ and $1 \times 10^{-12}\,{\rm g\,cm^{-3}}$).

collapse to 'interesting' densities, and any other initial conditions, for example a large $\beta_{\rm turb}$ will act to delay this.

Before considering the results using the RT scheme, we first consider how this differs from the barotropic equation of state. Here, we show six calculations where three sets of initial conditions have been solved using both the barotropic 'MHD' equation of state and the 'RMHD' algorithm. The addition of RT naturally causes heating of the fluid to occur unlike the fixed equation of state, as shown by the different relationship between the fluid density and specific internal energy for the radiative equation of state and the barotropic equation of state shown in Fig. 1. The way this translates into increased temperatures in the RT scheme is then shown by the temporal evolution of the maximum fluid temperature compared to the maximum density shown in Fig. 2. We note that the density appears to reach an approximate maximum slightly between $10^{-11}\,{\rm g\,cm^{-3}} < \rho < 10^{-10}\,{\rm g\,cm^{-3}}$ because of the insertion of a sink particle at (in this case) $\rho = 10^{-10}\,{\rm g\,cm^{-3}}$.

This increased temperature in turn promotes the formation of a larger pseudo-disc supported by the fluid pressure. In this paper, we use the same definition of pseudo-disc as in Lewis & Bate (2017). This is a disc-like object that rotates at sub-Keplerian speeds around a central object (and is therefore not a 'classical' accretion disc), but it is supported by the fluid pressure perpendicular to the plane of the disc against further collapse. As expected, the calculations proceed essentially identically, with the core centrally collapsing due to self-gravity, until the fluid density has risen significantly from its initial value. Fig. 3 demonstrates how the MHD and RMHD calculations are virtually indistinguishable at this evolutionary epoch. The $\mathcal{M} = 0.1$ and 0.3 calculations approach a maximum density of $\approx 10^{-10}\,{\rm g\,cm^{-3}}$ at $t \approx 1.02\,t_{\rm ff}$, whilst the $\mathcal{M} = 1.0$ calculation reaches a similar evolutionary point at $t \approx 1.14\,t_{\rm ff}$. After this, some divergence between the MHD and RMHD calcula-
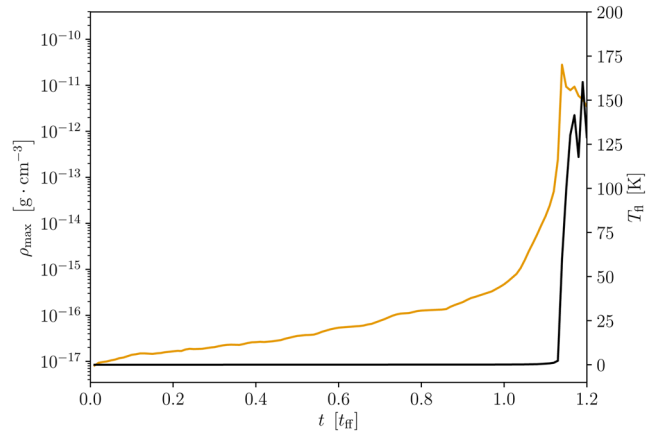

Figure 2. Evolution of the maximum fluid density (solid orange line) and maximum fluid temperature (solid black line) for $\mu = 5$ with a $\mathcal{M} = 1.0$ initial turbulence field. In the early phase of the calculation, when the maximum density in the cloud core is $\rho \ll 10^{-12}\,{\rm g\,cm^{-3}}$, the temperature of the core is effectively isothermal with $T = 13.8\,{\rm K}$. In this phase, the core is transparent to the radiation energy produced from the gravitational collapse and consequently negligible heating occurs. At higher densities, the fluid is heated and this energy is then transported by the RT scheme through the fluid.

tions can be seen. We also note that adding RT very slightly slows the collapse rate down, for instance the sink particle is inserted in the $\mathcal{M} = 0.1$ calculations $0.01\,t_{\rm ff}$ later. The additional thermal support provided by radiative feedback operates in a comparable way to how additional magnetic pressure opposes the gravitational collapse.

These results show that, even with very complicated initial conditions, the addition of radiation terms into calculations of collapsing cloud cores is important only at the shortest length-scales. Fig. 4 shows density projections of two pseudo-discs, one with RT and one with a barotropic equation of state. The addition of radiation promotes stability by allowing a larger pseudo-disc, with greater pressure support to form. For the remainder of this paper, we will consider the RMHD calculations only.

5 THE INITIAL PHASE OF THE COLLAPSE

Fig. 5 shows the evolution of the maximum density for three turbulent Mach numbers ($\mathcal{M} = 0.1$, 0.3, and 1.0) across three mass-to-flux ratios ($\mu = 5$, 10, and 20), which correspond to models μ05–M01(R), μ05–M03(R), μ05–M10(R), μ10–M01(R), μ10–M03(R), μ10–M10(R), μ20–M01(R), μ20–M03(R), and μ20–M10(R) in Table 1. As discussed in relation to Fig. 2, the fluid appears to reach a maximum density because of the insertion of a sink particle. Here, we see that the degree of turbulent support has a vastly greater influence on the collapse time of the core. Magnetic pressure support is extremely weak until the core reaches the highest densities and consequently decreasing the mass-to-flux ratio from, for example, 10 to 5 has a much smaller impact. We observed in Lewis & Bate (2017) and earlier in Lewis et al. (2015) that the initial field strength and geometry has an effect on the collapsing core, and we again see this effect here. There is (effectively) no magnetic pressure support along the field lines, and this is consequently the preferential direction for fluid to gravitationally collapse. Fig. 6 shows the evolution of three $\mu = 5$ cores and three $\mu = 20$ cores with $\rho_{\rm max} \approx 10^{-11}\,{\rm g\,cm^{-3}}$ where the characteristic 'oblate spheroid'
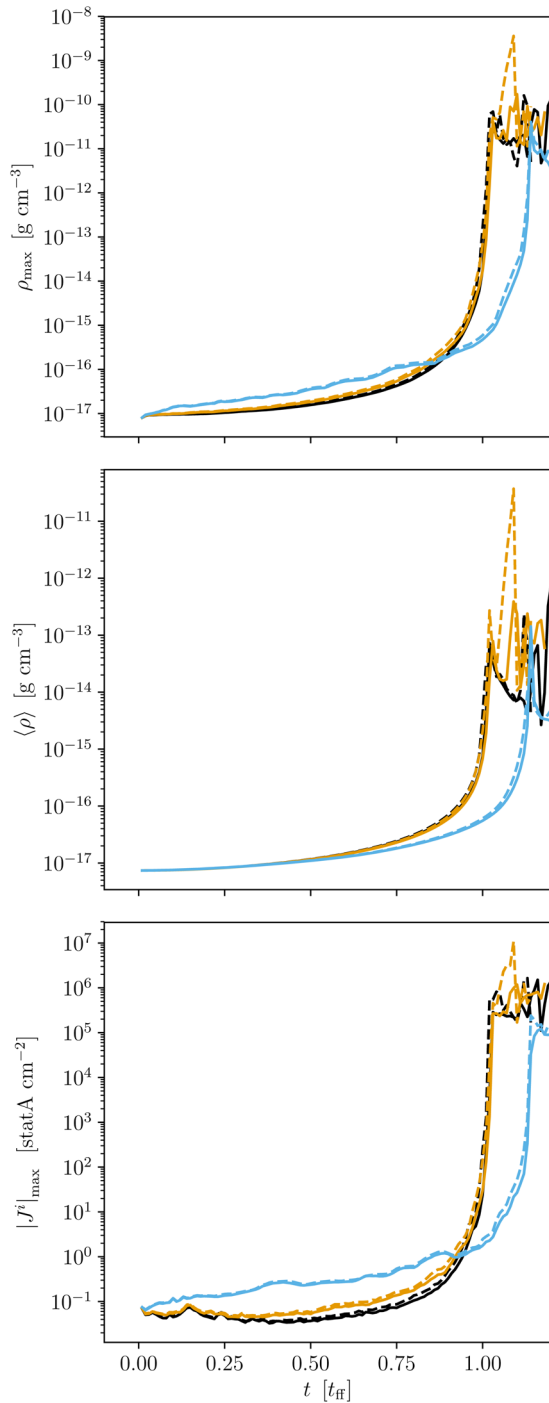
Figure 3. Evolution of maximum fluid density, ρ_{max}, mean fluid density, $\langle\rho\rangle$, and the maximum current density, $|J^i|_{max}$, for $\mathcal{M} = 0.1$, 0.3, and 1.0 (shown by the black, orange, and blue lines, respectively) turbulence calculations at $\mu = 5$ with both the radiative (solid lines) and barotropic (dashed lines) equations of state. The evolution until $\approx 1.00 t_{ff}$ is comparable for all four sub-sonic calculations, although the addition of radiation and the increase in the Mach number to 0.3 each delay the final collapse by $\approx 0.01 t_{ff}$. The two transonic calculations are also comparable until the final stage of the collapse, although there is an increased fluid density (and hence current density) in the early part of the calculation compared to the sub-sonic calculations due to the formation of turbulent structures.

shape proportional to the initial field strength can be clearly seen when the Mach number ≤ 0.3. We obtain a comparable range of ellipticities (i.e. axis ratios) to the laminar cores presented in Lewis & Bate (2017) with values of 0.6, 0.64, for $\mu = 5$, $\mathcal{M} = 0.1$ and 0.3 and 0.29, and 0.33 for $\mu = 20$ respectively, compared to 0.66 and 0.24 for a laminar core. Although the transonic $\mathcal{M} = 1$ cores are clearly somewhat oblate, it is not possible to demonstrate (due to the complex structure) that the $\mu = 20$ core has a lower oblateness than for $\mu = 5$. In any event, in this transonic regime, the turbulent kinetic energy – and hence the filament-like structures produced – has a much greater effect on the initial collapse than the magnetic field (cf. Fig. 5).

Once the core reaches densities of $\approx 10^{-10}\,\mathrm{g\,cm^{-3}}$, the magnetic field becomes a significant contributor to the subsequent evolution of the system. We do not include physical dissipative magnetic effects such as Ohmic resistivity or ambipolar diffusion. At densities in excess of $\approx 10^{-12}\,\mathrm{g\,cm^{-3}}$ magnetic dissipation can become important (Nakano 1976; Nakano, Nishi & Umebayashi 2002), however, in all the calculations presented here any substantial region with this high density will either be rapidly accreted or will form a sink particle. Consequently, neglecting these effects should not significantly impact the overall evolution of the pseudo-discs formed or any outflows produced. In addition, because of the RT scheme, radiation effects become important, as discussed earlier (see e.g. Fig. 2).

In summary, at high Mach numbers the turbulent velocity field dominates the initial phase of the evolution. RT becomes important when the density exceeds $\approx 10^{-13}\,\mathrm{g\,cm^{-3}}$. MHD effects in the initial phase are limited to changing the oblateness of the core, more complicated magnetic effects only occurring when the density is higher than about $10^{-11}\,\mathrm{g\,cm^{-3}}$. At lower Mach numbers, the turbulent velocity field instead acts to perturb and disrupt the uniformity of the collapse. This highlights a small difficulty in using the ideal free-fall time as a dimensionless temporal unit: the number of free-fall times at which the core will reach an 'interesting' density will vary depending on the sources of support against gravitational collapse present, for example a $\mathcal{M} = 1$ core will reach these densities $\sim \frac{1}{5} t_{ff}$ later than a laminar core. However, this unit is still useful for providing a dimensionless comparison between differing mass and volume cores. Consequently, in the following sections, we will in general synchronize the calculations so that a comparable evolutionary epoch is discussed, rather than a fixed t_{ff}.

6 SHAKEN: VARYING THE INITIAL MACH NUMBER

Fig. 7 shows the effect of increasing the initial turbulent velocity field for all three mass-to-flux ratios. A clear pattern emerges: first as in our previous laminar work, $\mu = 20$ calculations are unable to produce a bipolar outflow – which we see in the third column of Fig. 7. Secondly, that increasing the Mach number disrupts the system and inhibits the formation of a jet, as seen in the third and fourth rows of that figure. Throughout this paper, we adopt a similar classification to our earlier works. The term 'outflow' is used to describe *any* fluid propelled away from the protostellar core, whereas the term 'jet' is reserved for defined structures exhibiting at least some degree of collimation. A rotating pseudo-disc is a necessary precursor to the formation of a bipolar jet (see e.g. Price, Pringle & King 2003; Ciardi & Hennebelle 2010; Joos, Hennebelle & Ciardi 2012; Lewis et al. 2015) and an initially turbulent core acts to prevent the formation of this disc. Fig. 7 demonstrates
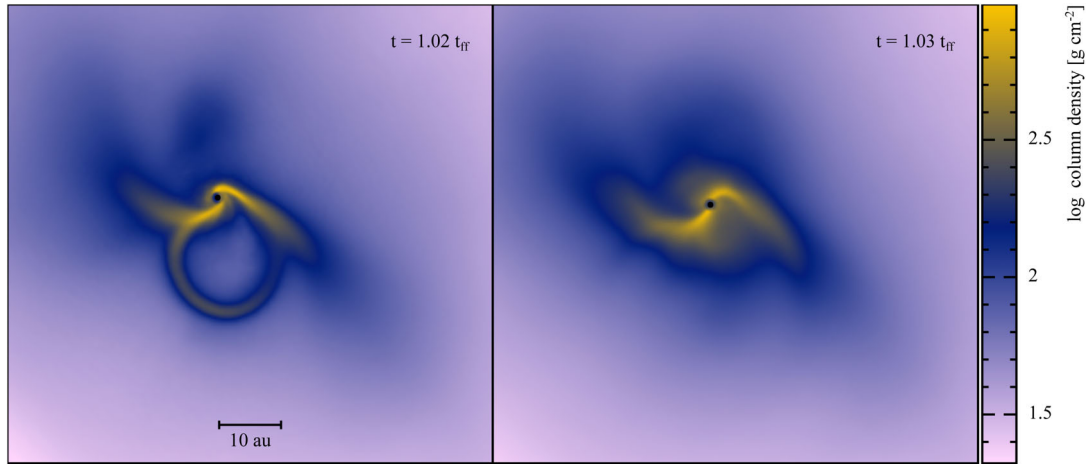
Figure 4. Column density projections in the z-direction for the $\mu = 5$, $\mathcal{M} = 0.1$ calculations. The left-hand panel shows the barotropic equation of state and the right-hand panel the RT scheme. A more extensive pseudo-disc with a radius of approximately 10 au has been produced by the RT calculation compared to the much smaller and more unstable disc on the left-hand panel. The barotropic equation of state produces a higher density and smaller pseudo-disc which may be more susceptible to gravitational instabilities. Alternatively, this ring-like structure may be caused by the magnetic interchange instability (see e.g. Spruit, Stehle & Papaloizou 1995; Lubow & Spruit 1995)
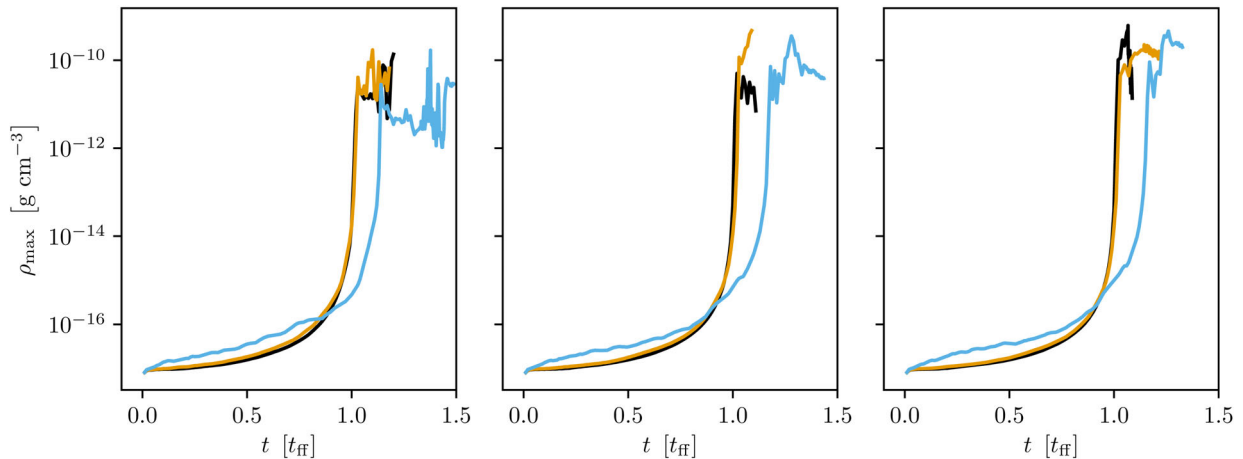
Figure 5. Evolution of the maximum fluid density for $\mathcal{M} = 0.1$ (solid black line), $\mathcal{M} = 0.3$ (short-dashed orange line), and $\mathcal{M} = 1.0$ (long-dashed purple line) initial turbulent velocity fields for an initial mass-to-flux ratio of $\mu = 5$ (left-hand panel), 10 (centre panel), and 20 (left-hand panel). For all three values of μ, increasing the initial turbulence velocity delays the collapse of the molecular cloud core by providing additional energy to support the core against gravity. An effective 'maximum' density is provided by the insertion of a sink particle at $\rho = 10^{-10} \mathrm{g\,cm^{-3}}$.

this effect: at $\mathcal{M} = 0.1$, the $\mu = 5$ and 10 calculations clearly exhibit disc structures similar to, though less uniform, those produced by laminar calculations, which are increasingly disrupted as the initial turbulent Mach number is increased. This effect is also present (albeit without the bipolar jets) for $\mu = 20$ (see also Joos et al. 2012). Fig. 8 compares the radially averaged azimuthal velocity of the three $\mathcal{M} = 0.1$ discs. We do not include more turbulent cores on this figure because the highly disrupted nature of the discs results in an impossibly confused graph. These results are broadly comparable with the conclusions of Matsumoto et al. (2017).

We also observe that adding RT to our laminar calculations does not markedly affect the shape or velocity of the outflow produced compared to the barotropic results obtained in Lewis & Bate (2017). This concurs with our observations in Section 4 (and also with Bate et al. 2014) that adding a RT treatment is a small overall effect, operating principally to produce a larger and warmer disc.

We now decompose the magnetic field into cylindrical components, [1] where

$$\begin{cases} r = \sqrt{x^2 + y^2} \\ \phi = \arctan \frac{y}{x} \\ z = z, \end{cases} \tag{33}$$

so that the magnetic field in this coordinate system is given by

$$\begin{cases} B_r = B_x \frac{x}{r} + B_y \frac{y}{r} \\ B_\phi = B_y \frac{x}{r} - B_x \frac{y}{r} \\ B_z = B_z. \end{cases} \tag{34}$$

---

[1] The form of this decomposition shown in equations (16)–(18) in Lewis & Bate (2017) was incorrect. However, the analysis and all plots used the correct equations as presented here.
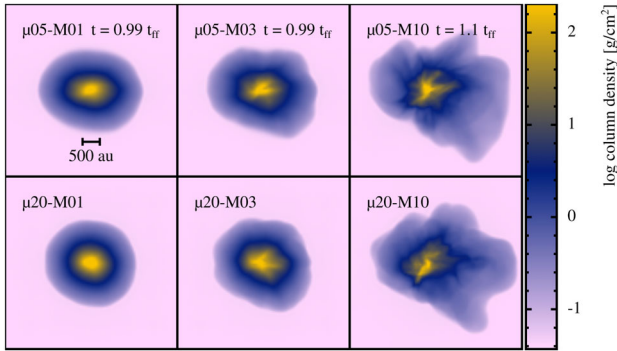
Figure 6. Column density projections for $\mathcal{M} = 0.1$, 0.3, and 1.0 calculations (left to right) with $\mu = 5$ (upper row) and $\mu = 20$ (lower row) showing how increasing the mass-to-flux ratio (and consequently decreasing the initial magnetic field) results in a less oblate core. This effect is less pronounced at higher turbulent Mach numbers where the structure of the core becomes dominated by the turbulent velocity field.

Then (e.g. as in Parker 1955), the azimuthal field, B_ϕ, and the toroidal field component are identical,

$$B_{\rm tor} = B_\phi, \tag{35}$$

and the magnitude of the poloidal component is given by

$$\left| B_{\rm p} \right| = \sqrt{B_{\rm r}^2 + B_{\rm z}^2}. \tag{36}$$

In Lewis & Bate (2017) , we concluded that the essential ingredients for collimated outflows were a strong poloidal field to lift material out of the disc–plane *coupled with* a strongly toroidal component to collimate the outflow. A solely torodial field trapped fluid in the disc and a solely poloidal field would produce a bulk outflow (cf. the 'detachment' seen for a $\mu = 10$ calculation in Lewis & Bate 2017 when the poloidal component overhauls the torodial one). In Fig. 9, we show how this effect is mirrored for these calculations. First, the sub-sonic $\mu = 20$ calculations have a strongly toroidal disc, with no significant region where the poloidal field dominates.

Conversely, the $\mu = 5$ and 10 calculations *with* an outflow have a poloidally dominated region which is then wound-up by the strongly toroidal disc (exemplified by the toroidal inner region of the jet). Clearly, then, by disrupting the formation of a pseudo-disc, turbulence is able to prevent angular momentum transport via a bipolar outflow. However, unlike for a laminar core, this does not lead to fragmentation. Whilst fragmentation can be suppressed in stronger fields ($\mu \geq 10$) by magnetic braking, hitherto we found that all $\mu = 20$ discs were gravitationally unstable and liable to fragment into binary or ternary systems. We note, however, that the increased turbulent velocity field has the effect of both making the (pseudo-)discs less massive and also placing less angular momentum in the disc. Both of these effects make the disc less vulnerable to fragmentation from gravitational–rotational torques. This latter point is echoed by comparing the total rotational energy of the whole core, which is reduced in the transonic cores compared to the sub-sonic ones as the turbulent motion acts to prevent simple rotation around the z-axis. We note also that the 'toroidal' region is a good tracer for the location of a pseudo-disc, albeit not the extent, since this region will extend out the edge of the core. For example, the transonic $\mathcal{M} = 1.0$ cores all develop discs which are neither flat nor close to perpendicular to the rotation axis (or equivalently perpendicular to the initial magnetic field axis).

The $\mu = 20$ calculations discussed in the preceding paragraph differ from the calculations presented in Lewis & Bate (2017) in an im-

portant way, viz. that here we include radiative transfer. This alone can prevent fragmentation of the core. However, to test whether the addition of turbulence alone can stop the fragmentation mode found in our previous work we also ran the $\mu = 20$, $\mathcal{M} = 1$ calculation *without* the RT treatment (this is calculation μ20–M10(M)). We show the results of this calculation alongside μ20–M00(R) (i.e. a laminar, radiative, $\mu = 20$ calculation) in Fig. 10. Here, we find that adding *either* radiation or turbulence is sufficient to stabilize the core against fragmentation into a multiple system. This indicates that the fragmentation mode proposed in Lewis & Bate (2017) can be suppressed by making a warmer disc or by a smaller disc (or both).

From this, we conclude that highly turbulent initial conditions are – all other things being equal – inimical to the formation of bipolar jets and well-defined pseudo-discs. This has consequences for observations: an observation that a very young protostellar object has a jet-like outflow implies that the core was initially sub-sonic.

7 STIRRED: VARYING THE INITIAL ANGULAR MOMENTUM

In Section 6 above, we showed that increasing the initial turbulent velocity field of the core into a transonic regime inhibits the formation of a (pseudo-)disc and therefore suppresses the formation of a bipolar outflow. Since disc structures are inherently connected with the angular momentum (or somewhat equivalently the rotational kinetic energy) in a collapsing core, we now take the $\mu = 5$ calculations with a $\mathcal{M} = 1.0$ velocity field and increase the initial rotation rate. These are calculations μ05–M10–r001(R) and μ05–M10–r002(R) in Table 1. μ05-M10(R) has $\beta_{\rm rot} = 0.005$, so these two calculations have double and quadruple the initial rotational energy (and hence the angular momenta are $\sqrt{2}$ and double the initial values) respectively.

Fig. 11 compares these three calculations at a similar evolutionary epoch. We find that μ05–M10–r001(R) (the calculation with double the initial angular momentum) has a very weak outflow, corresponding to a confused disc-like structure; however, μ05–M10–r002(R) produces a clear disc and a corresponding bipolar outflow. Fig. 12 clearly shows this, with a region of fluid moving the outward from the sink particle, i.e. where $v_z > 0$ for $z > 0$ (above the plane of the disc) and vice versa. We note that material undergoing a gravitational self-collapse invariably has $v_z \leq 0$ above the disc and vice versa. Unlike the sub-sonic cores presented above and the laminar cores presented in Lewis & Bate (2017), this outflow is much slower (ca. $|v_z| \approx 1 \,\mathrm{km\,s^{-1}}$) and much less substantial. The latter effect is shown by the reduced column density contrast between the outflow material and the surrounding cloud core.

The nature of any disc structure is related to the initial rotation rate. At the lowest initial rotation rate, i.e. calculation μ05–M10(R), no disc forms. Conversely at the highest rotation rate – calculation μ05–M10–r002(R) – a clear pseudo-disc has formed. However, this disc has a rotation speed slower than that seen in Fig. 8 for a sub-sonic core (and which is therefore even slower than a laminar core, e.g. μ05–M00(R)). This is the cause of the weaker outflow seen here. None the less, this illustrates that whilst turbulent kinetic energy can disrupt a core so much that it does not form a pseudo-disc, adding additional *rotational* energy can act to reform that disc structure. To quantify this effect, we define a new parameter,

$$\epsilon = \frac{\beta_{\rm turb}}{\beta_{\rm rot}} \equiv \frac{E_{\rm turb}}{E_{\rm rot}}, \tag{37}$$
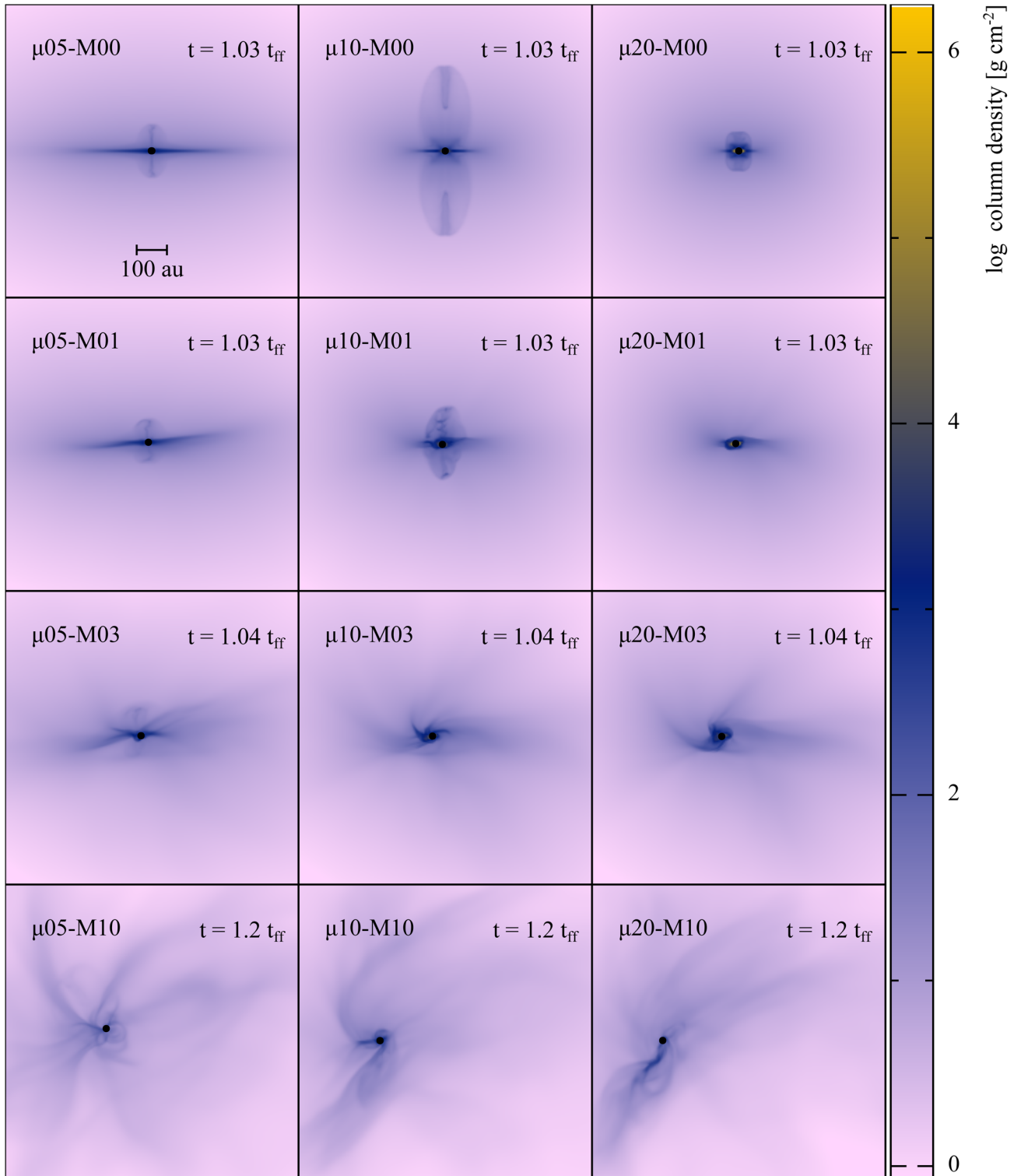
Figure 7. Column density projections in the *x*-direction for 12 RMHD calculations of a collapsing molecular cloud core, the time synchronization has been chosen so that the $\mu = 5$ calculations are an equivalent time after the insertion of a sink particle (which is coterminous with a maximum density being achieved). The left-hand column has an initial magnetic field strength given by $\mu = 5$, the central column has $\mu = 10$, and the right-hand column has $\mu = 20$. The initial turbulent Mach number increases down the page, with the uppermost row being laminar calculations where $\mathcal{M} = 0$, then $\mathcal{M} = 0.1, 0.3$ (sub-sonic cores), and 1.0 (transonic) in the bottom row. Bipolar outflows are only obvious for $\mu \leq 10$ coupled with $\mathcal{M} \leq 0.1$ although the $\mu = 5$, $\mathcal{M} = 0.3$ calculation has a weak outflow.

the conditions become more complicated. For example, a laminar core with a fully aligned magnetic field can produce an outflow with $|v_z| = 8\,\mathrm{km\,s^{-1}}$, a sub-sonic core where $\epsilon = 2.4$ produces a slower and less collimated outflow, but the transonic core with $\epsilon = 1.06$ only produces $|v_z| = 0.5\,\mathrm{km\,s^{-1}}$.

Fig. 13 shows the same poloidal–toroidal decomposition as in Fig. 9 but for the three $\mathcal{M} = 1$ calculations discussed in this section. The change between no outflow when $\epsilon = 26$ and a collimated jet when $\epsilon = 1.06$ is again shown in this analysis. There is also the hint of a weak outflow in the highly disrupted pseudo-disc when $\epsilon = 1.6$, however, the lack of a disc structure to collimate this suppresses a jet structure from being formed. This highlights how the formation of a disc is necessary to produce a jet-like outflow around a first hydrostatic core.

8 DISCUSSION

We observe that the ratio of the total magnetic, turbulent and rotational kinetic energies to the gravitational self-potential in the $\mathcal{M} = 1$ cores is very close to unity. Consequently, these cores are on the limit of boundedness and would become unbound with only a small increase in the turbulent velocities. This is consistent with the observed average velocities seen in cluster scale simulations, where cores (or comparable regions) undergoing a Jeans collapse are often sub-sonic, notwithstanding the initial highly supersonic velocities in the progenitor cloud (Klessen et al. 2000), and compatible with observed star formation regions, e.g. in Ophiuchus (Pattle et al. 2015).

A large value of ϵ in these highly turbulent (and weakly bound) cores is comparable to the strongly misaligned magnetic field and rotation axes that we explored in Lewis & Bate (2017). In those cases, values of the parameter $\vartheta \geq 60^{\circ}$ produced highly disrupted discs – with correspondingly slower rotation profiles – and this was fatal to the production of an outflow. The production of a bipolar jet from a first hydrostatic core is therefore linked to both having a suitable field strength and geometry (turbulence cannot make a weaker field more able to produce the necessary poloidal components to form a jet) to generate the outflow at all, combined with an environment conducive to the formation of a sub-Keplerian pseudo-disc. This former requirement is satisfied by having $\mu \leq 10$ and $\vartheta < 60^{\circ}$, whilst the latter requires $\epsilon \lesssim 1$ which implies either a sufficiently weak turbulent velocity field *or* a sufficiently strong rotational velocity field.

Observations of potential first hydrostatic core outflows (e.g. Dunham et al. 2011) report outflow speeds of around $|v_z| = 5\,\mathrm{km\,s^{-1}}$. These are consistent with the observed $|v_z|$ values seen for very weakly turbulent and laminar cores, where $\epsilon \ll 1$ but in these configurations the total kinetic energy is actually relatively low. Outflows are produced from much higher initial kinetic energies, i.e. when $\mathcal{M} = 1$, provided that $\epsilon \lesssim 1$. However, the outflow produced in this scenario – transonic turbulence coupled with additional angular momentum – is much slower. This has an important implication for observations, viz. that faster outflows are the result of less 'dynamic' initial conditions. Conversely, it also indicates that a slower outflow speed is a result of an elevated value of ϵ. This allows a limited degree of rewinding of the evolution of very young protostellar objects to predict the conditions in the Jeans unstable core from which they formed. The mass and size of the first hydrostatic core provides a limit on the maximum outflow and jet velocity (see Price et al. 2003). Therefore, simply trying to decrease ϵ to obtain faster jets is not possible, and objects such as MMS-6/OMC-3 found by

Figure 8. Radially averaged azimuthal velocity as a function of radius from the sink particle for the three $\mu = 5$, 10, and 20 calculations (black, orange, and blue solid lines, respectively) compared to the Keplerian velocity at that radius (dashed lines). The upper panel is for $\mathcal{M} = 0.1$ and the lower panel is for $\mathcal{M} = 0.3$. The pseudo-discs become progressively further from Keplerian as μ decreasing (i.e. as the field strength increases); in addition, for weaker fields increasing $\mathcal{M}$ also results in a more sub-Keplerian rotation profile.

such that $\epsilon > 1$ implies turbulence is the dominant source of kinetic energy, conversely $\epsilon < 1$ implies rotation is, and $\epsilon \approx 1$ implies approximate equality between the two fields. A value of $\epsilon \lesssim 1$ is a necessary pre-requisite for the formation of a pseudo-disc and outflow. The $\mu05$–M10(R) calculation has $\epsilon = 26 \gg 1$ and correspondingly the pseudo-disc was highly disrupted; conversely $\mu05$–M10–r002(R) had $\epsilon = 1.06 \approx 1$ and has formed a disc with a weak outflow. The intermediary phase $\mu05$–10–r001(R) has $\epsilon = 1.6$ which corresponds, as expected, to a disrupted pseudo-disc. These values are compatible with those obtained for lower Mach numbers, e.g. $\mu05$–M01(R) and $\mu05$–M03(R) have $\epsilon = 0.26 < 1$ and $\epsilon = 2.4 \approx 1$ respectively (identical values are necessarily obtained for $\mu10$–01(R), etc.).

Comparing the outflow velocities between the earlier laminar cores, the sub-sonic cores in Section 6 and the transonic cores in this section, we find a steady decrease in the outflow speed, $|v_z|$, as
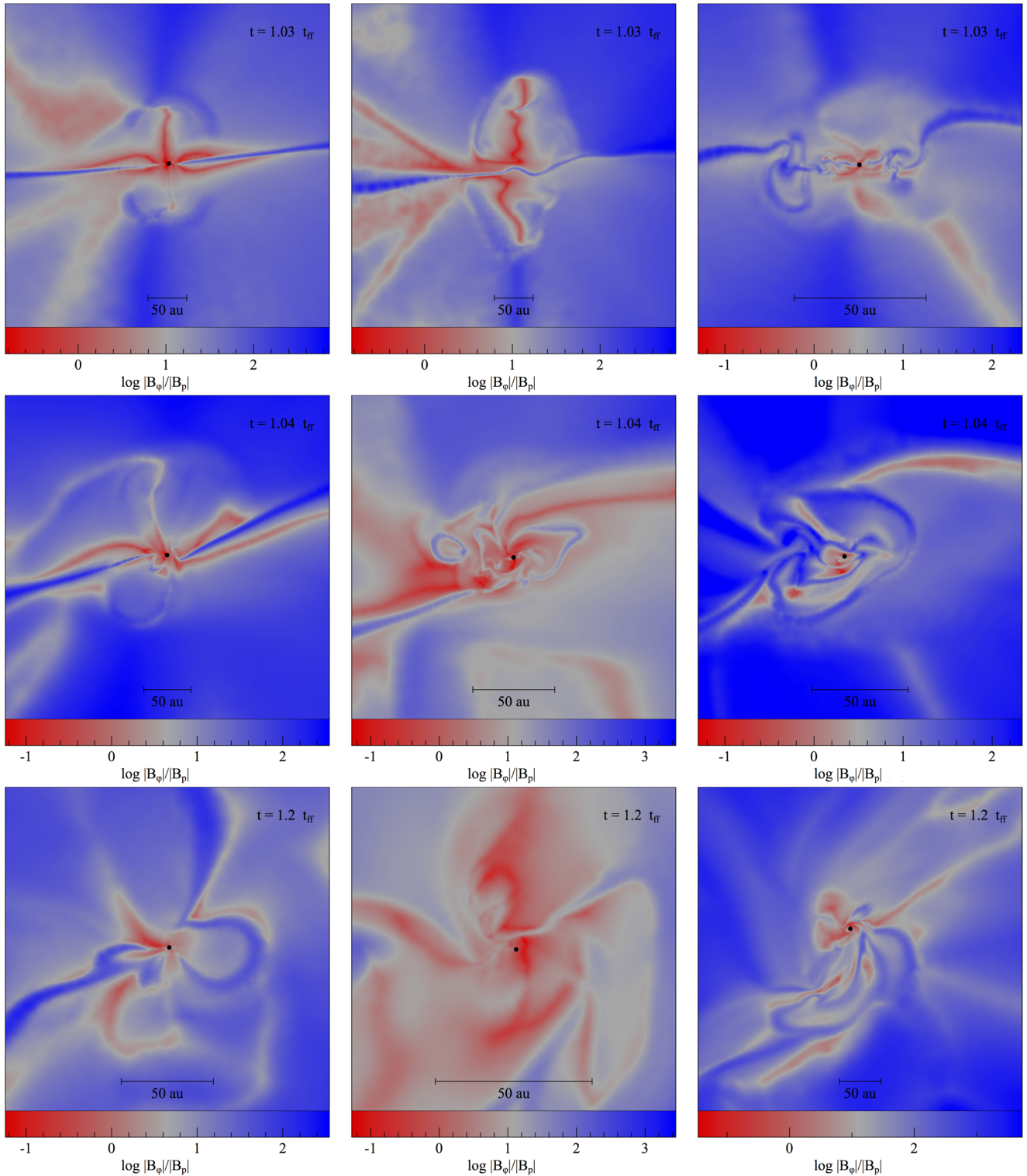
Figure 9. Transverse sections, in a *z*–*x* plane through the sink particle of the ratio of the poloidal magnetic field component to the toroidal component for all nine turbulent calculations presented in Fig. 7. The sections are presented in the same order as in that figure, so that the top middle and bottom rows are $\mu = 5$, 10, and 20 respectively and the left-hand, centre, and right-hand columns are $\mathcal{M} = 0.1$, 0.3, and 1.0, respectively. Red indicates regions where the poloidal field component [cf. equation (36)] is dominant and conversely blue indicates regions where the toroidal field [cf. equation (35)] is dominant. Material is removed from the region around the sink particle by the poloidal field. This process, however, is more efficient and results in a collimated jet – in particular as seen in the top left panel – when the toroidal field is able to wind up the material as it is being lifted away from a pseudo-disc.
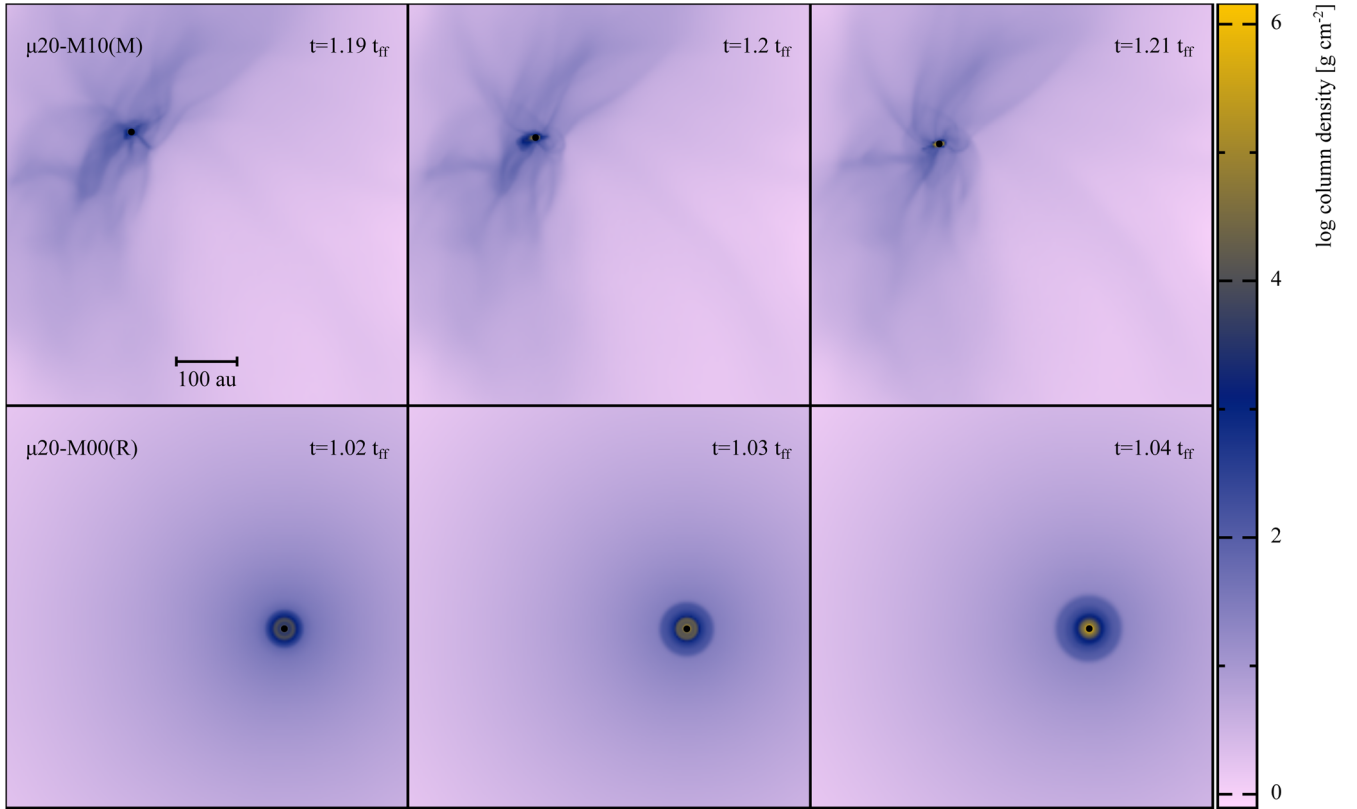
Figure 10. Column density projections in the *y*-direction for μ20–M10(M) (upper row) and μ20-M00(R) (lower row) at a comparable evolutionary epoch after a sink particle is inserted. Neither calculation has fragmented, unlike the $\mu = 20$ calculations in Lewis & Bate (2017), demonstrating that adding *either* turbulence (see the upper row) or RT (lower row) is sufficient to prevent this fragmentation mode.

Takahashi & Ho (2012) or the Herbig–Haro object HH 1165 found by Riaz et al. (2017) are more evolved than the first core phase.

We noted earlier that our results are broadly comparable with Matsumoto et al. (2017). For example, in the initial phase of the collapse, we obtain a similar link between oblateness and field strength, and disruption of the collapsing core by higher Mach numbers (see also Matsumoto & Hanawa 2011). However, Matsumoto et al. (2017) use significantly stronger magnetic fields ($1.12 \leq \mu \leq 2.81$). The core mass used there was also higher than our work ($M_{core} = 2.51 \, M_{\odot}$ as opposed to $1 \, M_{\odot}$), so this implies a much stronger magnetic field is present. We obtain a similar reduction in the radius of the pseudo-disc as μ is reduced as in that paper, however, because we also probe much weaker field strengths – $\mu \geq 20$ – we also find that once magnetic effects are reduced further the disc size again decreases due to reduced angular momentum transport (Lewis & Bate 2017). The difference in magnetic field strengths also explains the lack of any magnetic pressure induced 'cavity' in our calculations. We also note that our calculations include an RT scheme and begin with uniform density, not Bonnor–Ebert, spheres.

We find a strong, but not perfect, alignment between our pseudo-discs and the outflow produced. This is likely due to the way we superimpose a random turbulent velocity and a solid-body rotation profile together. This guarantees that the angular momentum vector of the system will be very closely aligned to the *z*-axis (which is also the magnetic field axis). In comparison, an approach whereby the random seed used to generate the turbulence is used to produce angular momentum will result in a more complicated angular momentum vector. Consequently, in such a system misalignments between the discs and outflows are more likely to occur. However,

our approach has the advantage that it is possible to separate linear and rotational effects more easily. Keeping the rotational component of the velocity field separate would also allow the effect of varying ϑ to be more readily explored. We note, however, that the partially asymmetrical appearance of the outflow when $\mathcal{M} = 1$ and $\epsilon \gg 1$ is compatible with the complex structure of HH 1165 (Riaz et al. 2017), and in particular the asymmetrical nature of the outflow seen in that system. This indicates that the combination of rotational effects – to create a disc and outflows – and turbulence is necessary to explain the complex structures seen in protostars.

9 CONCLUSIONS

We performed 18 smoothed particle magnetohydrodynamical calculations of the collapse of a molecular cloud core. Four of these calculations used a barotropic equation of state; the remaining 14 use an FLD RT scheme. These calculations use mass-to-flux ratios ranging from $5 \leq \mu \leq 20$, initial turbulent Mach numbers $0 \leq \mathcal{M} \leq 1$ and initial rotation rates corresponding to $0.005 \leq \beta_{rot} \leq 0.02$.

Calculations using RT produces a smoother distribution of thermal energy and hence promote the formation of larger, warmer, discs compared to the barotropic equation of state. Consequently, the use of a full RMHD scheme is desirable in calculations of protostellar collapses.

We obtain a strong link between the degree of turbulence in the initial molecular core and the nature of the consequent outflow. Laminar, $\mathcal{M} = 0$, cores (now with RT) produce results comparable to our earlier work (see Lewis & Bate 2017) with a strong
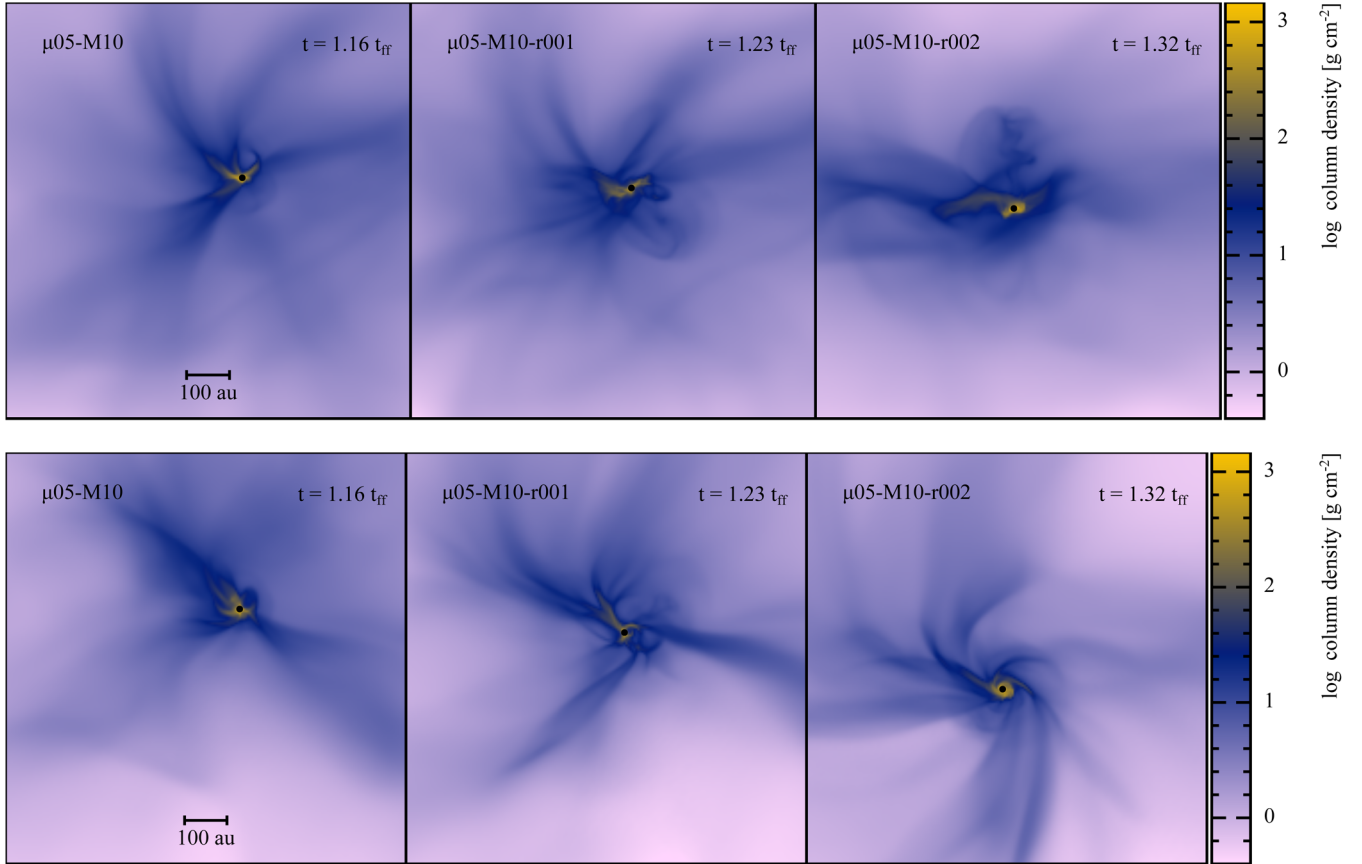
Figure 11. Column density projections in the *x*-direction (upper row) and *z*-direction (lower row) for three RMHD calculations of a collapsing molecular cloud core, all with $\mu = 5$ and an initial Mach number of 1.0. The left-hand panel is the same calculation presented in Section 6, shown here again as a comparison, which has $\beta_{\rm rot} = 0.005$. The centre and right-hand panels then have $\beta_{\rm rot} = 0.01$ and 0.02, i.e. double and quadruple, respectively.
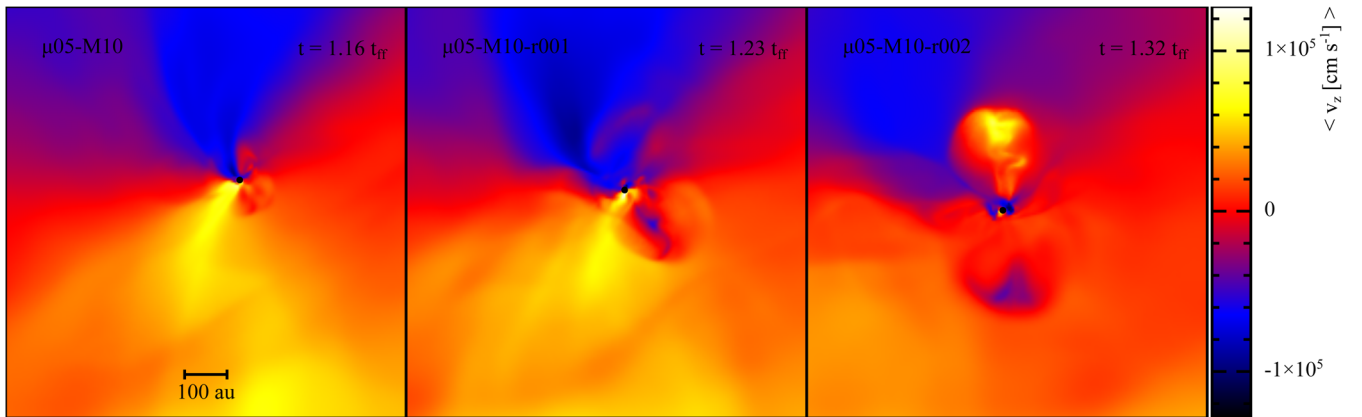

Figure 12. Density-weighted average of the *z*-component of the velocity field for the three calculations presented in Fig. 11, i.e. where the left-hand, centre, and right-hand panels have $\beta_{\rm rot} = 0.005$, 0.01, and 0.02, respectively. The signature of an outflow, a region with material moving the 'wrong way' is clearly visible in the right-hand panel, as opposed to the highly disrupted calculations presented in the other two panels.

$|v_z| \simeq 5\,{\rm km\,s^{-1}}$ bipolar jet and outflow for strong magnetic fields ($\mu \leq 10$). No collimated or substantial outflow is produced for $\mathcal{M} = 0$, $\mu = 20$. At the other extreme, when $\beta_{\rm rot} = 0.005$ as before, but $\mathcal{M} = 1$ the calculation is highly disrupted and no outflow is produced for all field strengths. The addition of turbulence or RT, or both, can also stabilize a $\mu = 20$ core against fragmentation into binary or ternary systems.

We then increase the initial rotation rate from $\beta_{\rm rot} = 0.005$ to 0.02 for $\mathcal{M} = 1$. The additional angular momentum promotes the formation of a disc when the ratio of turbulent kinetic to rotational kinetic energy, $\epsilon \lesssim 1$. Once such a disc is formed, we again find that an outflow is produced albeit with a slower velocity of $|v_z| \simeq 1\,{\rm km\,s^{-1}}$ and with some asymmetries. We therefore conclude that the velocity of a first hydrostatic core outflow is related to this ratio,
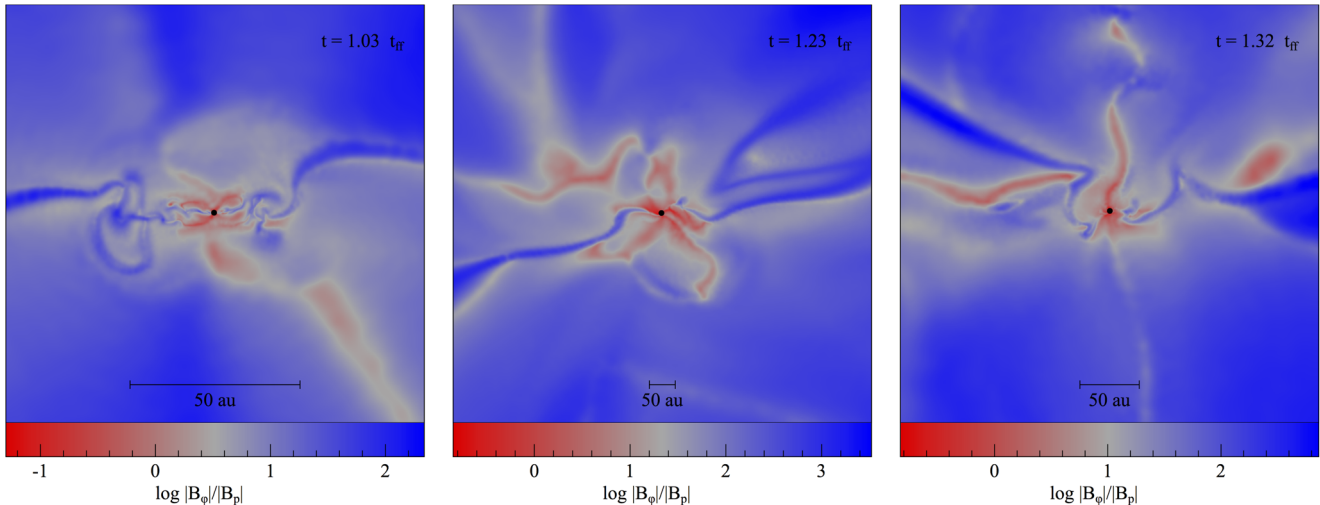
Figure 13. Transverse sections, in a *z–x* plane through the sink particle of the ratio of the poloidal magnetic field component to the toroidal component for the three calculations presented in Fig. 11. As in Fig. 9, red indicates regions where the poloidal field component dominates compared to blue regions where the toroidal field is dominant.

ϵ, and that faster outflows are correlated with lower values of ϵ and vice versa.

The output files from the SPH code used for the calculations presented in this paper have been placed in the University of Exeter's Open Research Exeter (ORE) repository and can be accessed via the handle http://hdl.handle.net/10871/32288 or by the DOI: https://doi.org/10.24378/exe.203.

REFERENCES

Alexander D. R., 1975, ApJS, 29, 363
André P. et al., 2010, A&A, 518, L102
Banerjee R., Pudritz R. E., 2006, ApJ, 641, 949
Bate M. R., 2009, MNRAS, 392, 590
Bate M. R., 2012, MNRAS, 419, 3115
Bate M. R., Burkert A., 1997, MNRAS, 288, 1060
Bate M. R., Bonnell I. A., Price N. M., 1995, MNRAS, 277, 362
Bate M. R., Bonnell I. A., Bromm V., 2003, MNRAS, 339, 577
Bate M. R., Tricco T. S., Price D. J., 2014, MNRAS, 437, 77
Benz W., 1988, Comput. Phys. Commun., 48, 97
Benz W., 1990, in Buchler J. R., ed., Numerical Modelling of Nonlinear Stellar Pulsations Problems and Prospects. Kluwer, Dordrecht, p. 269
Benz W., Bowers R. L., Cameron A. G. W., Press W. H., 1990, ApJ, 348, 647
Black D. C., Bodenheimer P., 1975, ApJ, 199, 619
Bonnor W. B., 1956, MNRAS, 116, 351
Burkert A., Bodenheimer P., 2000, ApJ, 543, 822
Børve S., Omang M., Trulsen J., 2001, ApJ, 561, 82
Ciardi A., Hennebelle P., 2010, MNRAS, 409, L39
Crutcher R. M., 2012, ARA&A, 50, 29
Dedner A., Kemm F., Kröner D., Munz C.-D., Schnitzer T., Wesenberg M., 2002, J. Comput. Phys., 175, 645
Dunham M. M., Chen X., Arce H. G., Bourke T. L., Schnee S., Enoch M. L., 2011, ApJ, 742, 1
Ebert R., 1955, Z. Astrophys., 37, 217
Elmegreen B. G., 1993, ApJ, 419, L29
Federrath C., Roman-Duval J., Klessen R. S., Schmidt W., Mac Low M.-M., 2010, A&A, 512, A81
Federrath C., Sur S., Schleicher D. R. G., Banerjee R., Klessen R. S., 2011, ApJ, 731, 62
Fehlberg E., 1969, NASA Technical Report, R-315
Gingold R. A., Monaghan J. J., 1977, MNRAS, 181, 375
Goodman A. A., Benson P. J., Fuller G. A., Myers P. C., 1993, ApJ, 406, 528
Heyer M. H., Brunt C. M., 2004, ApJ, 615, L45
Heyer M., Dame T. M., 2015, ARA&A, 53, 583
Hily-Blant P., Teyssier D., Philipp S., Güsten R., 2005, A&A, 440, 909
Hosking J. G., 2002, PhD thesis, University of Cardiff
Hunter J. D., 2007, Comput. Sci. Eng., 9, 90
Jeans J. H., 1902, Phil. Trans. R. Soc., 199, 1
Joos M., Hennebelle P., Ciardi A., 2012, A&A, 543, A128
Klessen R. S., Heitsch F., Mac Low M.-M., 2000, ApJ, 535, 887
Kuruwita R. L., Federrath C., Ireland M., 2017, MNRAS, 470, 1626
Larson R. B., 1969, MNRAS, 145, 271
Larson R. B., 1981, MNRAS, 194, 809
Levermore C. D., Pomraning G. C., 1981, ApJ, 248, 321
Lewis B. T., Bate M. R., 2017, MNRAS, 467, 3324
Lewis B. T., Bate M. R., Price D. J., 2015, MNRAS, 451, 4807
Lewis B. T., Bate M. R., Tricco T. S., 2016, in Hu X., ed., Proceedings of the 11th International SPHERIC Workshop. Technische Universität München, Germany

Li Z.-Y., Krasnopolsky R., Shang H., 2013, ApJ, 774, 82
Lubow S. H., Spruit H. C., 1995, ApJ, 445, 337
Lucy L. B., 1977, AJ, 82, 1013
Mac Low M.-M., Klessen R. S., 2004, Rev. Mod. Phys., 76, 125
Machida M. N., Inutsuka S.-i., Matsumoto T., 2006, ApJ, 647, L151
Machida M. N., Inutsuka S.-i., Matsumoto T., 2007, ApJ, 670, 1198
Machida M. N., Inutsuka S.-i., Matsumoto T., 2008, ApJ, 676, 1088
Matsumoto T., Hanawa T., 2011, ApJ, 728, 47
Matsumoto T., Tomisaka K., 2004, ApJ, 616, 266
Matsumoto T., Machida M. N., Inutsuka S.-i., 2017, ApJ, 839, 69
McKee C. F., Ostriker E. C., 2007, ARA&A, 45, 565
Men'shchikov A. et al., 2010, A&A, 518, L103
Monaghan J. J., 1985, J. Comput. Phys., 60, 253
Monaghan J. J., 1997, J. Comput. Phys., 136, 298
Morris J. P., Monaghan J. J., 1997, J. Comput. Phys., 136, 41
Motte F., André P., 2001, A&A, 365, 440
Mouschovias T. C., Spitzer L., Jr, 1976, ApJ, 210, 326
Myers P. C., 2009, ApJ, 700, 1609
Nakano T., 1976, PASJ, 28, 355
Nakano T., Nishi R., Umebayashi T., 2002, ApJ, 573, 199
Ostriker E. C., Stone J. M., Gammie C. F., 2001, ApJ, 546, 980
Padoan P., Nordlund Å., 2002, ApJ, 576, 870
Pandey B. P., Wardle M., 2008, MNRAS, 385, 2269
Parker E. N., 1955, ApJ, 122, 293
Pattle K. et al., 2015, MNRAS, 450, 1094
Planck M. K. E. L., 1914, Vorlesungen uber die Theorie der Warmestrahlung. "The Theory of Heat Radiation". Dover, Mineola, NY, United States
Pollack J. B., McKay C. P., Christofferson B. M., 1985, Icarus, 64, 471
Pound M. W., Reipurth B., Bally J., 2003, AJ, 125, 2108
Price D. J., 2007, PASA, 24, 159
Price D. J., 2011, Astrophysics Source Code Library, record ascl:1103.004
Price D. J., Bate M. R., 2007, MNRAS, 377, 77
Price D. J., Monaghan J. J., 2004a, MNRAS, 348, 123
Price D. J., Monaghan J. J., 2004b, MNRAS, 348, 139
Price D. J., Monaghan J. J., 2005, MNRAS, 364, 384
Price D. J., Monaghan J. J., 2007, MNRAS, 374, 1347
Price D. J., Pringle J. E., King A. R., 2003, MNRAS, 339, 1223
Price D. J., Tricco T. S., Bate M. R., 2012, MNRAS, 423, L45
Riaz B., Briceno C., Whelan E., Heathcote S., 2017, ApJ, 844, 47
Roberts W. W., 1969, ApJ, 158, 123
Shu F. H., 1977, ApJ, 214, 488
Spruit H. C., Stehle R., Papaloizou J. C. B., 1995, MNRAS, 275, 1223
Takahashi S., Ho P. T. P., 2012, ApJ, 745, L10
Tomida K., Okuzumi S., Machida M. N., 2015, ApJ, 801, 117
Tomisaka K., 2002, ApJ, 575, 306
Tricco T. S., Price D. J., 2012, J. Comput. Phys., 231, 7214
Tricco T. S., Price D. J., 2013, MNRAS, 436, 2810
Tricco T. S., Price D. J., Bate M. R., 2016, J. Comput. Phys., 322, 326
Tsukamoto Y., Iwasaki K., Okuzumi S., Machida M. N., Inutsuka S., 2015, ApJ, 810, L26
van der Walt S., Colbert S. C., Varoquaux G., 2011, Comput. Sci. Eng., 13, 22
Ward-Thompson D. et al., 2010, A&A, 518, L92
Whitehouse S. C., Bate M. R., 2006, MNRAS, 367, 32
Whitehouse S. C., Bate M. R., Monaghan J. J., 2005, MNRAS, 364, 1367
Wurster J., Price D., Ayliffe B., 2014, MNRAS, 444, 1104
Wurster J., Price D. J., Bate M. R., 2016, MNRAS, 457, 1037

This paper has been typeset from a TEX/LATEX file prepared by the author.